

Controlled probing of localization effects in non-Hermitian Aubry-André model via topoelectrical circuits

Dipendu Halder^{1,*} and Saurabh Basu^{1,†}

¹*Department of Physics, Indian Institute of Technology Guwahati-Guwahati, 781039 Assam, India*

Anderson localization (AL) and the non-Hermitian skin effect (NHSE) are two distinct confinement phenomena of the eigenfunctions, that are, respectively, driven by disorder and non-reciprocity. Understanding their interplay within a unified framework offers valuable insights into the localization properties of low-dimensional systems. To this end, we investigate a non-Hermitian (NH) version of the celebrated Aubry-André (AA) model, which serves as an ideal platform due to its unique self-dual properties and ability to demonstrate localization-delocalization transition in one dimension. Interestingly, in our setting, the competition between AL and NHSE can be precisely controlled via the complex phase of the quasiperiodic disorder. Additionally, by analyzing the time evolution, we demonstrate quantum jumps between the NH-induced skin states and the AL states to occur in the system. Further, to gain support for our theoretical predictions in an experimental platform, we propose a topoelectrical circuit, featuring an interface that separates two distinct electrical circuit networks. The localization properties of our model can be studied by analyzing the voltage profile (VP) of the circuit. The VP exhibits confinement at the interface, analogous to the NHSE, while the phenomenon of AL can be perceived via the localization of the VP in the vicinity of the excitation node where the power supply is connected. This interplay leads to a spatially tunable localization of the VP. Our findings provide deeper insights into the controlled confinement of the eigenstates of the NH AA model by designing analogous features in topoelectrical circuits that should open avenues in the fabrication of advanced electronic devices, such as highly sensitive sensors and efficient information transfer systems.

I. INTRODUCTION

Disorders, impurities, and defects are inherent properties of material preparation. A particularly intriguing phenomenon linked to disorder in condensed matter physics is the Anderson localization [1] (AL), which describes how an infinitesimal random disorder induces a transition from an extended to a localized phase in a system in any dimension less than three. Interestingly, AL is not limited to systems with random disorder; quasiperiodic (QP) disorders with incommensurate periods can also result in AL. Among the various QP models, the Aubry-André (AA) model [2] has garnered significant attention for its theoretical elegance [3–5] and experimental realizations in platforms like photonic crystals [6–8], ultra-cold atoms [9, 10], and superconducting circuits [11]. A hallmark of the AA model is the absence of mobility edges, that is, an energy-dependent localization transition in the system. This robustness makes the AA model an excellent platform for exploring localization phenomena.

In recent years, on a parallel framework, non-Hermitian (NH) phenomena have experienced remarkable growth, finding applications across a wide range of condensed matter systems [12–15]. This exciting area has unveiled a wealth of novel physical phenomena, such as the non-Hermitian skin effect (NHSE) [16–20], where the bulk eigenstates accumulate near the boundaries, and the emergence of exceptional points [21, 22], where the Hamiltonian becomes defective with the eigenvalues and the eigenvectors being coalesced. Additionally, the non-Bloch band theory [16, 23] has redefined the conventional Bloch theorem, offering new insights into the wave

behavior of NH systems. Experimental advancements have validated these phenomena in diverse physical scenarios, including ultra-cold atoms [24, 25], mechanical systems [26], acoustic systems [27–29], etc. These developments have established NH systems as apt avenues for exploring the interplay between topology and non-hermiticity.

Furthermore, the interplay between disorder and non-hermiticity has also gained significant attention, particularly with the proposal of Hatano-Nelson model in 1996 [30]. Through the tight-binding (TB) framework, this one-dimensional (1D) model, characterized by asymmetric hopping and random disorder, reveals the localization-delocalization transition. Subsequently, NH QP systems have also emerged as a vibrant research focus [31–38]. These systems reveal fascinating physics by highlighting the interplay between the NHSE, driven by non-reciprocity, and the AL, induced by quasiperiodicity. Among various experimental platforms, topoelectrical circuits (TECs) have evolved as a powerful tool in experiments, drawing attention for their ability to map TB Hamiltonians onto circuit Laplacians [39–44]. By adjusting electrical components and connection configurations, TECs offer remarkable flexibility to engineer and explore a wide range of topological characteristics. This unique adaptability enables precise control over the system parameters, providing an unprecedented playground for fine-tuning topological phenomena. In TECs, topological edge states are revealed through the impedance or voltage profiles, which can be measured by exciting specific nodes within the circuit network. These features make TECs an excellent medium for studying both theoretical and experimental aspects of topology in condensed matter systems. While there exists a sizable literature on TEC in realizing the NHSE [45–50] and AL in QP systems [51–55] individually, the intricate interplay between these phenomena remains largely unexplored.

In this work, we examine the competition between the AL

* corresponding author: h.dipendu@iitg.ac.in

† saurabh@iitg.ac.in

and the NHSE, along with their time evolution, proposing a design of a TEC that serves as a direct classical analog of these quantum localization phenomena. Starting with a 1D NH AA model featuring an interface, separating two non-equivalent AA chains, we notice an emergence of intriguing phenomena arising out of the interplay between AL and NHSE. Utilizing standard circuit elements, we construct a TEC capable of replicating both the Hermitian and NH versions of the AA model. Hence, by exciting a random node with an external source, we successfully observe the classical analogs of both AL and NHSE. A striking phenomenon emerges when these two compete in a TEC, offering enhanced control over their time evolution. The novelty of our approach lies in the ability to precisely manipulate the localization of the voltage profile (VP) to specific nodes or ranges within the circuit network, as well as the ability to control the amplitude of the VP.

The paper is organized as follows: Section II introduces the

$$H = \sum_{k=1}^{L_0} \left[(t + \gamma) \hat{c}_{k+1}^\dagger \hat{c}_k + (t - \gamma) \hat{c}_k^\dagger \hat{c}_{k+1} \right] + \sum_{k=L_0+1}^{2L} \left[(t - \gamma) \hat{c}_{k+1}^\dagger \hat{c}_k + (t + \gamma) \hat{c}_k^\dagger \hat{c}_{k+1} \right] + \sum_{k=1}^{2L+1} \lambda_k \hat{c}_k^\dagger \hat{c}_k; \quad \lambda_k = 2\lambda \cos(2\pi\beta k + i\alpha), \quad (1)$$

where t , γ , and λ denote the strengths of the nearest-neighbor hopping, non-reciprocity, and QP disorder, respectively. All of these parameters are assumed to be real and positive. Note that, all parameters in this TB model are in the unit of t . Our system comprises of $(2L + 1)$ lattice sites, and $(L_0 + 1)^{\text{th}}$ site marks the position of the interface (L_0 is a variable), starting from the first node. For example, if we choose $L_0 = L$, we have two non-equivalent NH AA chains of the same length that differ via the sign of the non-reciprocity parameter, γ . The parameter α introduces a complex component to the QP potential and plays a pivotal role in the localization-

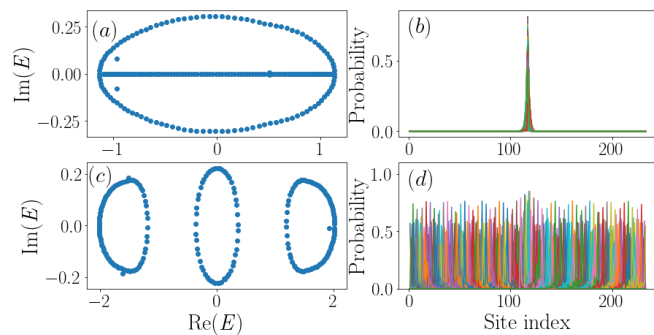


FIG. 1. Numerical analyses for a total number of lattice sites, $(2L + 1) = 233$, being a Fibonacci number, with $t = 0.65$ and $\gamma = 0.35$ are presented. (a) Real vs Imaginary parts of the energy spectra for $\lambda = \alpha = 0$; (b) Probability distribution of the corresponding eigenstates, which localize at site index $(L + 1) = 117$. (c) Same as (a) but with $\lambda = 0.9$, $\alpha = 0.2$. (d) The skin states in (b) have now become AL states as $\alpha > \alpha_c \simeq 0.105$.

theoretical TB framework, outlining the fundamental physics. In section III, we investigate the time evolution of the AA model when excited at an arbitrary site. Section IV explores the electrical analogs of AL and NHSE in the TEC through voltage measurements performed using LTspice software by *Analog Devices* [56]. This section also examines the interplay between AL and NHSE within the TEC. Finally, section V summarizes our findings and discusses potential experimental realizations or device implementations inspired by our theoretical framework.

II. THEORETICAL MODEL

We adopt the non-reciprocal version of the NH AA model introduced by S. Longhi [31], incorporating an interface at a particular lattice site of the chain. The Hamiltonian (in 1D) is given by,

delocalization transition of our model. Its prominence will become evident in the subsequent discussions. β is an irrational number given by $\beta = (\sqrt{5} - 1)/2$ with β^{-1} being the golden ratio. It is obtained via $\beta = \lim_{n \rightarrow \infty} \left(\frac{F_{n-1}}{F_n} \right)$, where the Fibonacci numbers F_n s are defined recursively by $F_{n+1} = F_n + F_{n-1}$ and $F_0 = F_1 = 1$. The operators \hat{c}_k and \hat{c}_k^\dagger denote the annihilation and creation operators for spinless fermions at the site k .

The behavior of the system depends on two distinct scenarios: (a) $\lambda = 0$: in the absence of the QP potential, the system reduces to the clean Hatano-Nelson model (without any disorder). Here, NHSE arises due to the non-reciprocal hopping parameter γ . (b) $\lambda \neq 0$, $\alpha \neq 0$ but $\gamma = 0$: the model reduces to a reciprocal NH AA model that includes a complex QP potential with the introduction of α . In the Hatano-Nelson model without an interface, all the bulk states accumulate at one of the edges; which is determined by the sign of the non-reciprocity parameter, γ [20]. The energy spectra for the periodic and open boundary conditions are markedly different, with the former creating closed loops in the complex plane that encloses the energy spectra corresponding to the open chain, which lies along the real axis. For concreteness, we set $L_0 = L$ in H (Eq. (1)) for further discussions and circuit design. Fig. 1(a) depicts the energy spectra of H with $\lambda = 0$. The system exhibits exactly $(L + 1)$ real energy eigenvalues, while the remaining (L) eigenvalues are complex, a stark contrast to the clean Hatano-Nelson model without an interface. The probability distribution of the corresponding eigenstates is shown in Fig. 1(b). These eigenstates localize at exactly the interface (at the middle of the chain).

In the presence of the QP potential ($\lambda \neq 0$, $\alpha \neq 0$) along

with $\gamma \neq 0$, the spectrum displays a hierarchical structure of three bands, as illustrated in Fig. 1(c). In the case of $\gamma = \alpha = 0$, the system undergoes an AL transition at $\lambda = t$ [57], governed by the self-duality of the model. This property ensures that the system is either fully extended or fully localized, dictated solely by the QP potential strength, λ . The introduction of α modifies this behavior, shifting the AL transition to a critical value of α , which is $\ln |t/\lambda|$. This occurs because all the localized eigenstates in the self-dual space share a uniform inverse localization length of $\ln |\lambda/t|$ [31]. With $\alpha = 0$ but $\gamma \neq 0$, the localization transition instead occurs at $\lambda = \max(t + \gamma, t - \gamma)$ [51]. Using Avila's global theory [58], Li *et al.* [38] demonstrated that for a generalized scenario ($\alpha \neq 0, \gamma \neq 0$), the AL transition occurs at

$$\alpha_c = \ln |\max(t + \gamma, t - \gamma)/\lambda| \quad (2)$$

The above results are summarized in Table I. Also, Fig. 1(d) highlights this scenario through the probability distribution of eigenstates for a high value of α ($\alpha > \alpha_c$), where the AL dominates the NHSE. Additionally, the study of localization and topological phase transitions in generalized AA models with incommensurately modulated asymmetric hopping amplitudes offers valuable insights [35, 36].

TABLE I. The table presents the analytically determined localization-delocalization transition points as functions of the two NH parameters, namely, α (the imaginary phase of the quasiperiodic potential) and γ (the non-reciprocity parameter in the hopping amplitude t).

NH parameters	$\alpha = 0$	$\alpha \neq 0$
$\gamma = 0$	$\lambda_c = t$	$\alpha_c = \ln t/\lambda $
$\gamma \neq 0$	$\lambda_c = \max(t + \gamma, t - \gamma)$	$\alpha_c = \ln \max(t + \gamma, t - \gamma)/\lambda $

III. TIME EVOLUTION OF THE NH AA MODEL

We have explored the localization properties of the eigenstates of the Hamiltonian for the NH AA model given by Eq. (1). An intriguing question arises: does the interplay between the NHSE and the AL persist over long time scales, or does the time-evolved system unveil any interesting physics? To address this, we investigate the time evolution of an excited wavefunction in the NH AA model. Let the initial wavefunction at $t = 0$ be $|\Psi(x, 0)\rangle$, which can be expanded as a linear combination of the eigenstates of H in Eq. (1), given as,

$$|\Psi(x, 0)\rangle = \sum_{q=1}^{2L+1} a_q(0) \psi_q(x), \quad (3)$$

where $a_q(0)$ is the coefficient corresponding to the q^{th} eigenstate (ψ_q) at $t = 0$, and is responsible for the time evolution of the initial wavefunction, $|\Psi(x, 0)\rangle$. Note that x is a discrete variable and lies in the range $x \in [1, 2L + 1]$. As, the eigenstates, $\psi_q(x)$ of H form a complete orthonormal basis, we can

express $a_q(0)$ and $a_q(t)$ as,

$$\begin{aligned} a_q(0) &= \langle \psi_q(x) | \Psi(x, 0) \rangle \\ \Rightarrow a_q(t) &= \langle \psi_q(x) | \Psi(x, 0) \rangle e^{-\frac{iE_q t}{\hbar}}, \end{aligned} \quad (4)$$

for any q , where E_q is the eigenvalue corresponding to the eigenvector, $\psi_q(x)$. Now, as an initial condition, we choose a delta-type excitation of the form,

$$|\Psi(x, 0)\rangle = \delta(x - m) \quad (5)$$

which is localized entirely at the m^{th} site and is zero elsewhere. The time evolution of $|\Psi(x, 0)\rangle$ from Eqs. (3) and (4), can be expressed as,

$$|\Psi(x, t)\rangle = \sum_{q=1}^{2L+1} \langle \psi_q(x) | \Psi(x, 0) \rangle e^{-\frac{iE_q t}{\hbar}} \psi_q(x). \quad (6)$$

However, this equation is specifically applicable to systems without boundaries, where x ranges from $-\infty$ to $+\infty$. Hence, assuming that the wavefunction yields vanishing probability density at the edges of the chain, any reflection of the state during its evolution is thereby precluded. Subsequently, we can reliably use Eq. (6) to determine $|\Psi(x, t)\rangle$ for any finite range of x at all subsequent times.

NH systems are known for their non-conservation of energy, leading to non-unitary time evolution. As a result, these systems violate probability conservation, resulting in the norm of the wavefunction to either grow or diminish as a function of time. Thus, we have to normalize the amplitude of the evolved wavefunction with its norm at each time step. Thus, the evolution of the wavefunction over a small interval dt occurs through a two-step process [59]. First, the wavefunction

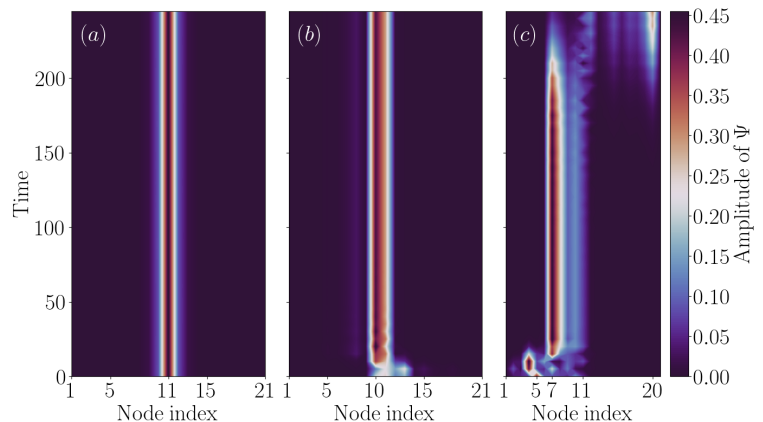


FIG. 2. The temporal evolution of the excitation in the non-reciprocal NH AA model is illustrated for three scenarios: (a) $\lambda = 0$, (b) $\lambda = 1$, $\alpha = 0.425$, and (c) $\lambda = 1$, $\alpha = 0.9$. In the first case, the localization of the wavefunction at the interface is attributed to the NHSE. In the second case, at $\alpha = \alpha_c$, a slight shift in the localization is observed. Finally, for a much larger value of α , the wavefunction undergoes brief transitions, namely, from the 5th site to the 4th site, then to the 7th site for an extended period, and ultimately localizes at the 20th site.

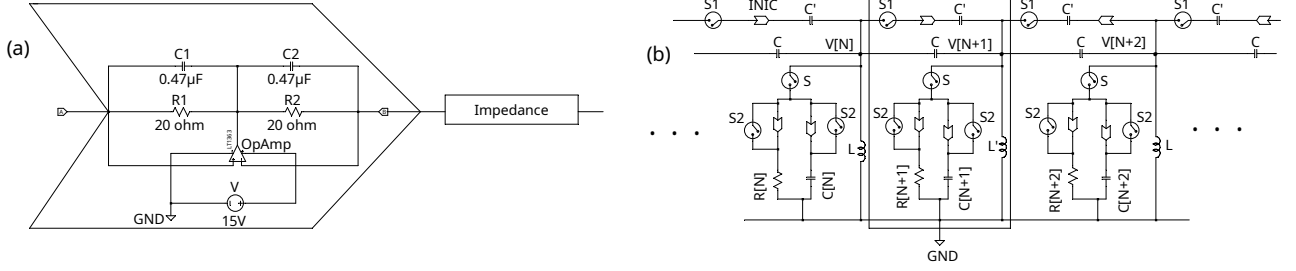


FIG. 3. (a) Circuit diagram of an impedance converter with current inversion (INIC) is shown. The current entering the INIC from the left(right) side experiences a negative(positive) impedance placed in the rectangular box. (b) The TEC diagram corresponds to the non-reciprocal NH AA model. The rectangular box highlights the $(N + 1)^{\text{th}}$ node. $V[N]$ denotes the output voltage at N^{th} node.

evolves as,

$$|\Psi(x, t + dt)\rangle = e^{-\frac{iHdt}{\hbar}} |\Psi(x, t)\rangle. \quad (7)$$

This is hence followed by a normalization step,

$$|\Psi(x, t + dt)\rangle = \frac{|\Psi(x, t + dt)\rangle}{\| |\Psi(x, t + dt)\rangle \|}, \quad (8)$$

where $\|\cdot\|$ denotes the norm.

Let us now employ Eqs. (7) and (8) to numerically analyze $|\Psi(x, t)\rangle$. As an example, we excite the delta-type wavefunction at the 5th site, that is, $m = 5$ in Eq. (5). Fig. 2(a) illustrates the NHSE observed at the interface in the absence of any QP potential ($\lambda = 0$). Fig. 2(b) represents the system at a critical value of α , given by $\alpha_c = \ln |\max(t+\gamma, t-\gamma)/\lambda| \simeq 0.425$ for $\lambda = 1$. At this point, the eigenstates of H undergo a transition from exhibiting NHSE to AL, and the localization of the time-evolved wavefunction starts to shift away from the interface. For $\alpha > \alpha_c$, $|\Psi(x, t)\rangle$ no longer remains localized at the interface, as shown in Fig. 2(c). Instead, the wave propagates via quantized jumps between the AL states located randomly at distinct sites of the chain, a phenomenon termed as ‘NH jumps’ [60–62]. These jumps are distinctive artefacts of the NH disorder, incorporated in our case via the parameter α . Thus, the time evolution of the wavefunction involves several NH jumps over a certain time frame, as depicted in Fig. 2(c). The jumps can be predicted with the help of both the initial wavefunction $|\Psi(x, 0)\rangle$, and $a_q(t)$. Note that, $a_q(t)$ in turn depends on the corresponding eigenvalues, given by Eq. (4).

IV. TEC CONSTRUCTION

Similar to the Hamiltonian of a TB model, electrical circuit networks operate based on their Laplacians, which govern the network’s response at each node [63]. For an electrical network with N_0 nodes, let \mathcal{L} represent the Laplacian, and V_i and I_i denote the voltage and the total current through an external source at the i^{th} node. According to Kirchhoff’s law,

the following relation holds,

$$I_i = \sum_{p(i \neq p)}^{N_0} X_{ip}(V_i - V_p) + X_i V_i \quad \text{for } i = 1, 2, 3, \dots, N_0, \quad (9)$$

where X_{ip} is the conductance between i^{th} node and p^{th} node. Note that X_{ii} has no physical meaning and is set to zero, while X_i represents the resultant conductance between i^{th} node and the ground. With these definitions, Eq. (9) can be expressed as $I = \mathcal{L}V$, where \mathcal{L} is the $N_0 \times N_0$ Laplacian matrix with elements, $\mathcal{L}_{ip} = -X_{ip} + \delta_{ip}W_i$, where $W_i = \sum_p X_{ip} + X_i$. Thus, the Laplacian \mathcal{L} mirrors a particular second-quantized Hamiltonian of a TB model based on the arrangement of the circuit components, such as capacitors, inductors, resistors, operational amplifiers (opamps), etc.

A. TEC: NH AA model

Now, we focus on forming an analog circuit corresponding to the TB model given by Eq. (1). To achieve the goal, the Laplacian of the circuit must accurately replicate the Hamiltonian at the resonant frequency, f_R , of the circuit. The intersite hoppings can be modeled by capacitors (C), while the non-reciprocity in the hoppings (γ) is introduced via INIC (impedance converter with current inversion) in the circuit. As shown in Fig. 3(a), for the realization of the INIC, an op-amp is employed that works in the negative feedback regime. To ensure the stability of the circuit, two 20Ω resistors are placed in parallel to the capacitors [45]. The resonant frequency of the circuit is given by,

$$f_R = \frac{1}{2\pi\sqrt{2LC}} \simeq 5191 \text{ Hz}; \quad \omega_R = \frac{1}{\sqrt{2LC}}, \quad (10)$$

with $L = 10 \mu\text{H}$ and $C = 47 \mu\text{F}$. All these values are standard for commercial uses and are kept fixed throughout this work. The real and the imaginary parts of the QP potential, λ_k in Eq. (1), are represented by node-dependent capacitors ($C[k]$) and resistors ($R[k]$), respectively, with $|\text{Re}(\lambda_k)| \equiv \omega_R C[k]$, and $|\text{Im}(\lambda_k)| \equiv R[k]^{-1}$. Here, k denotes the node index and is analogous to the site index of Eq. (1). The switches for the

circuit elements are denoted by S and $S1$. The circuit also includes master switches for S and $S1$ (not shown in Fig. 3(b)), which control all the S and $S1$ switches across the circuit. For instance, the master switch for S ($S1$) can simultaneously open or close all S ($S1$) switches. However, this functionality does not extend to $S2$, as $S2$ is specifically designed to alter the signs of $C[k]$ or $R[k]$ based on the values of λ_k , which, in turn, depend on the node index, k . The total number of nodes is $(2N + 1) = 21$, which is kept fixed through the rest of the analysis. It is worth noting that 21 nodes are sufficient to obtain reliable results from the TEC framework using LTspice software [56], which provides realistic results that align closely with experimental observations. The detailed mathematical rigor behind the formation of the Laplacian of this TEC is provided in Appendix A. To get results in support of the theoretical results in Fig. 1, we have to obtain the eigenvectors of the Laplacian in terms of measurable quantities like the voltage or the impedance profile. However, to do that, every node must be excited via a current (or a voltage) source, which shall make the process unnecessarily complicated. Instead, a more practical approach is to excite a single node using a current (or a voltage) source and simulate the voltage response of the TEC using the LTspice software. The calculations still allow us to observe the localization of the VP, which is equivalent to NHSE, and AL in the TB model, as shown in Figs. 1(b) and 1(d), respectively. Interestingly, both these phenomena are tunable in our TEC. The detailed analysis of the time evolution of the excitation is explained in Appendix B.

B. NHSE in TEC

To realize and explore the NHSE in the non-reciprocal circuit, we open (disconnect) the master switch for all the S switches and close (connect) the master switch for all the $S1$ switches in Fig. 3(b), thereby configuring the TEC to replicate the clean Hatano-Nelson model. To demonstrate a voltage build-up at the interface, we excite the 3rd node with a voltage pulse of amplitude 1 mV for a duration of 10 μs and record the output signal at each node for 3000 μs . To effectively analyze the output, we calculate the root mean square (rms) values of the voltage signal at suitable time intervals for each node. It is important to note that we have indeed verified that all the relevant phenomena are captured with this time range (3000 μs). Thus, for this particular setup, the observations are made till $t = 3000 \mu\text{s}$, which corresponds to the maximum value along the y -axis (representing time). Using LTspice, these data are visualized in a colormap representing the VP as a function of time in Fig. 4. The results show that the VP localizes at the interface, specifically at 11th node, as illustrated in Fig. 4. This behavior closely reflects the NHSE observed in the NH AA model (see Fig. 1(b)). Moreover, this interface localization of the VP serves as a direct representation of the time-evolved wavefunction in the TB model (see Fig. 2(a)), where the delta excitation at the 5th site ultimately localizes at the 11th site. The grounded inductors at the edges have a distinct value of $L_{\text{edge}} \simeq 62 \mu\text{H}$, while the inductor at the 11th node, representing the interface, is chosen as $L' \simeq 6 \mu\text{H}$. These values

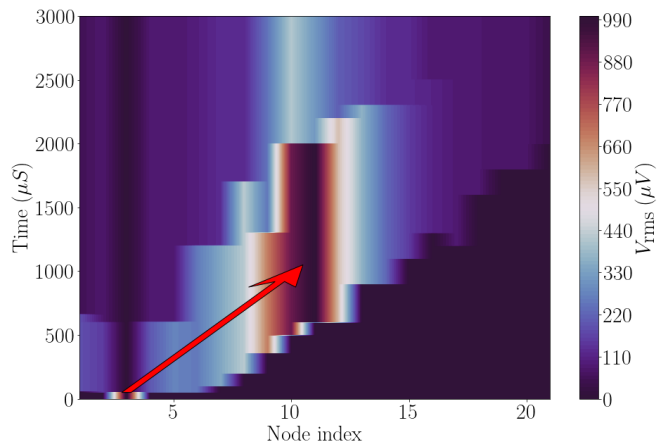


FIG. 4. Colormap of the rms values of the output VP as functions of both time and node index is shown. Commencing around time equal to 500 μs and continuing until approximately 2000 μs , the VP becomes localized at the interface, whose location occurs at the 11th node. The red arrow illustrates the progression of the excitation from the 3rd node to the interface over time.

differ from the other grounded inductors, $L (= 10 \mu\text{H})$. The role of the non-reciprocity parameter, γ , is implemented using $C' (= 32 \mu\text{F})$ along with an INIC (see Fig. 3(b)). The mapping between the TB model and the circuit is thus established via the relations $(t \pm \gamma) \equiv \omega_R(C \pm C') \simeq (1.53 \pm 1.04)$. Recently, Liu *et al.* [46] demonstrated NHSE at the interface in TECs for both 1D and 2D systems by employing a voltage follower, where the current flows unidirectionally, instead of using an INIC. Both approaches are well-accepted and provide reliable results for constructing non-reciprocal circuits.

Let us briefly summarize the measurement process and the data acquisition thereafter using LTspice. Users can select from LTspice's built-in device models or define their own. To construct a circuit in the software, elements from its library (or customized models) are placed on the schematic to obtain a desired circuit diagram, followed by appropriate connections. Once assembled, the circuit is simulated to observe its response under various conditions, including the presence or absence of external sources. It is important to note that LTspice presents the node voltages and currents through circuit elements as functions of time using a graphical interface.

Let us now illustrate the measurement procedure to generate Fig. 4 and its production from the raw data obtained from LTspice. Since the excitation (voltage pulse) at the 3rd node is short-lived and vanishes after 10 μs , localization for a short duration appears at the 3rd node in Fig. 4 when the voltage is measured. Consequently, the circuit's response is temporally constrained, implying that the output voltage at any node decays with time due to the presence of dissipative elements, such as the resistors (embedded within the INIC). This makes smooth measurement of the voltage as a function of time (at very short intervals) challenging. Therefore, the most effective approach is to measure the rms values of the output over non-equivalent discrete time intervals. For instance, the output voltage at the 11th node (interface) is measured at the fol-

lowing time intervals: (i) $0 - 600 \mu\text{s}$, (ii) $600 - 2000 \mu\text{s}$, and (iii) $2000 - 3000 \mu\text{s}$. These chosen time intervals vary from node to node, depending on where the output signal reaches its maximum amplitude and how long it is sustained before decaying. This measurement process is responsible for the appearance and disappearance of the voltage localization occurring in a stepwise manner, observed in Fig. 4. Furthermore, the data along the z -axis, representing the rms values of output voltages at different nodes and time intervals, are linearly interpolated using Python programming language to ensure smooth transitions while preserving the integrity of the raw data obtained from LTspice.

Interestingly, no signal is detected at the 11th node up to $600 \mu\text{s}$, as the rms value of the output voltage in this interval is nearly zero. However, during the $600 - 2000 \mu\text{s}$ interval, the rms value increases significantly, leading to the ‘dark’ region (approximately $990 \mu\text{V}$) in Fig. 4. Alternatively, this can be understood by noting that, initially excited at the 3rd node, the signal requires $600 \mu\text{s}$ to reach the interface at the 11th node, represented by the red arrow, and hence, no output signal is observed at the 11th node before $t = 600 \mu\text{s}$. Similarly, in the $2000 - 3000 \mu\text{s}$ interval, the rms output voltage diminishes due to dissipation in the circuit. This localization occurs regardless of the node of excitation and the pulse amplitude of the pulse (or the form of the pulse, such as square, triangular, etc.), demonstrating the robustness of the phenomenon. Interestingly, it parallels the phenomenon of ‘topological funneling of light,’ where a light field within a photonic mesh lattice with an interface is directed toward the interface, irrespective of their shape or the input location [64].

C. AL in TEC

As depicted in Fig. 3(b), to isolate and observe the AL, we close the master switch for S , while keeping $S1$ open. The only practical technique to incorporate the onsite QP potential in the circuit is to place the capacitors and resistors obeying the following equations, namely,

$$C[k] = -\text{Re}(\lambda_k)/\omega_R = -2\lambda \cos(2\pi\beta k) \cosh \alpha/\omega_R, \quad (11)$$

$$R[k] = [\text{Im}(\lambda_k)]^{-1} = [-2\lambda \sin(2\pi\beta k) \sinh \alpha]^{-1}, \quad (12)$$

derived from the expression for λ_k in Eq. (1). It is crucial to note that both $\text{Re}(\lambda_k)$ and $\text{Im}(\lambda_k)$ being oscillatory functions, can assume negative values, and consequently, $C[k]$ and $R[k]$ may be negative. To avoid negative capacitance values, a capacitor of constant value can be grounded [55], ensuring no impact on the central results. However, this strategy is not feasible for resistors ($R[k]$), as additional grounded resistors would unnecessarily increase dissipation in the circuit. As a remedy, we make the resistors negative using INIC. While INIC primarily ensures non-reciprocal current flow between the nodes, when one node is grounded (as is the case in our setup), it does not affect the circuit’s Laplacian and yields the desired outcomes. Therefore, the absolute values of $C[k]$ and $R[k]$ are placed at each node based on the values of $|\text{Re}(\lambda_k)|$

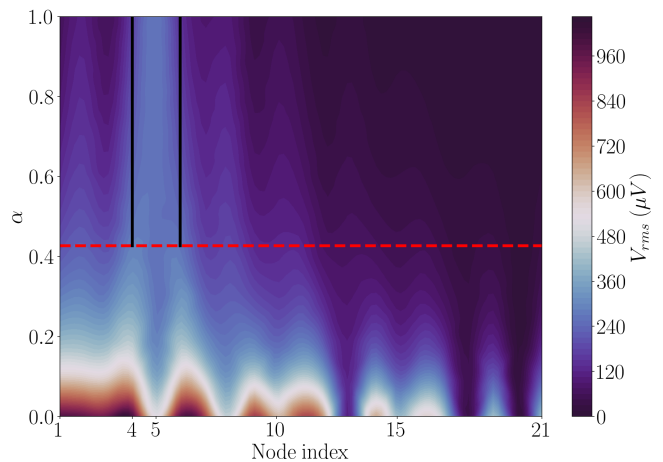


FIG. 5. The rms values of the output signal, measured over the duration from $600 \mu\text{s}$ to $2000 \mu\text{s}$, are presented as functions of the node indices and α . The red dashed line denotes the critical value of α , namely, α_c , obtained from Eq. (2). The two black vertical lines indicate the localization of the VP at the 5th node for $\alpha > \alpha_c$.

and $|\text{Im}(\lambda_k)|$, respectively. $S2$ switches are carefully toggled (closed or opened) at each node to fix the signs of $\text{Re}(\lambda_k)$ and $\text{Im}(\lambda_k)$. Moreover, the grounded inductors at the edges have a value of $L_{\text{edge}} = 20 \mu\text{H}$, while L' is identical to L as there exists no interface in this case.

Fig. 5 illustrates the VP of this TEC setup, analogous to the reciprocal NH AA model, as a function of α , with $\lambda = 1$ in Eq. (1). A constant current source of amplitude 1 mA and frequency f_R , as defined in Eq. (10), is applied at the 4th node. This leads to a smooth variation of VP, in contrast to the stepwise pattern observed in Fig. 4. As a consequence, there is no need to compute the rms value of the output voltage over different time segments for different nodes. For the NH AA model, the AL transition should occur at the critical value $\alpha_c = \ln |t/\lambda|$, calculated using Eq. (2), with $\gamma = 0$. The red dashed line in the figure marks this critical value, $\alpha_c \simeq 0.425$. However, due to practical factors such as the finite system size (only 21 nodes being considered) and simulational limitations of LTspice, a sharp transition is not observed. Nevertheless, the results demonstrate that for $\alpha > \alpha_c$, the VP becomes predominantly localized at the 5th node. When our simulation is repeated by considering excitation at different nodes (not shown here), the localization consistently occurs in the vicinity of the respective excitation node, thus highlighting a predictable and robust localization center. The predictability sharply contrasts the phenomenon of NH jumps observed in our TB model in Fig. 2(c), where wave packet evolution transpires not through gradual diffusion, but through sudden transitions between the distinct states. This discrepancy arises from the nature of the input excitation, as the time evolution of the voltage profile is highly sensitive to the form of the initial stimulus, thoroughly discussed in Appendix B. While the NH jumps in the NH AA model result from the spontaneous evolution of an initially localized delta-type wavefunction, the VP localization for the TEC in Fig. 5 emerges under a steady

sinusoidal current source.

D. Competition between AL & NHSE in TEC

The interplay between NHSE and AL in the NH AA model exhibits fascinating behavior in localization transition. AL directs a single-site excitation toward a ‘focal point,’ determined by the weight factors based on the overlap between the initial excitation and exponentially localized eigenstates [60], while NHSE drives it to an interface (or the edges). To probe deeper into this interplay in the TEC, we close both S and $S1$ to incorporate both the non-reciprocity and the QP potential and again excite the 4th node with a current source, as described earlier. Fig. 6(a) shows that when the QP disorder is real ($\alpha = 0$), the disorder potential is weak compared to the non-reciprocity parameter (γ) and is unable to drive the signal towards the excitation node. However, once α surpasses the critical value $\alpha_c \simeq 0.54$ (determined using Eq. (2)), the localization of the output voltage shifts to the excitation (4th) node. The VP for $\alpha = 1$ represents the analogous scenario in the TEC corresponding to the NH AA model depicted in Fig. 1(d). An intriguing aspect of this behavior is that the output amplitude diminishes with increasing α . This behavior is attributed to the significant rise in $|R[k]|$, which scales as $[\sinh \alpha]^{-1}$ (Eq. (12)). Consequently, by tuning α , one can effectively manipulate both the spatial localization and the amplitude of the output signal. This dual ability to modulate the NHSE and the AL dynamics is a distinctive feature of our TEC with potential applications similar to information transfer communication devices or the development of highly sensitive sensors.

Upon closer inspection, a gradual increase in α , from zero to α_c while keeping λ fixed ($\lambda = 1.5$ in this case) unveils a peculiar phenomenon. In the TEC, as previously discussed, AL is spatially confined over a short range near the excitation node. On the other hand, NHSE drives the excitation towards the interface. This interplay generates a fascinating *tug-of-war* scenario between the NHSE and the AL-induced localization, resulting in a ‘partial’ delocalization of the output signal within a certain spatial range. This range is bounded by two controllable key nodes, namely, the interface (11th) and the excitation (4th) node. Fig. 6(b) illustrates this phenomenon, where the VP shows non-zero oscillations between the 4th and the 11th nodes, beyond which VP decays to zero. During the transition, the amplitude of the output signal becomes somewhat uniform across the intermediate nodes, effectively creating a spatial channel for the signal. Furthermore, the position and width of this channel can be tuned by altering the excitation node or the interface of the circuit, offering versatile control over the behavior of the input signal to propagate. Thus, as said earlier, α serves as a critical parameter, acting as a switch that toggles between the phenomenon of NHSE and AL on the spreading dynamics of a single-site excitation.

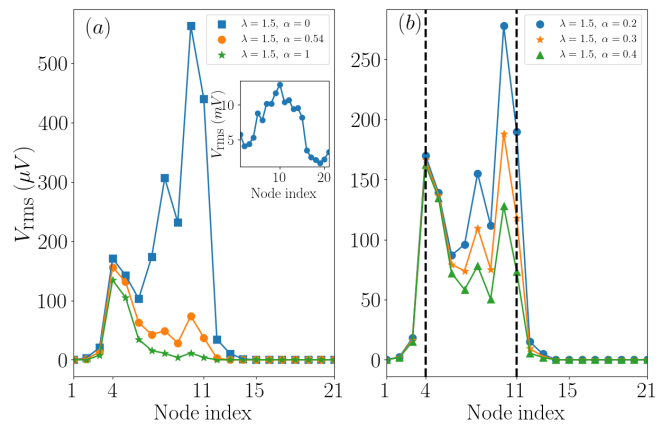


FIG. 6. (a) The rms values of the VP are plotted for different values of α for $\lambda = 1.5$, measured over the duration $1000 \mu\text{s}$ to $3000 \mu\text{s}$. The VP moves towards the 4th node at $\alpha = \alpha_c$ with a much smaller amplitude. The inset depicts the VP in the absence of any QP potential $\lambda = 0$, measured over the duration $2000 \mu\text{s}$ to $5000 \mu\text{s}$. Note that all the values are in mV, which suggests voltage amplification, compared to the constant external signal, for a sufficiently longer time. (b) The same profile, but for values of α between zero and the critical value (α_c). The two black-dashed vertical lines enclose the key nodes (exciting and interface nodes), that contain the partial delocalization of the VP.

V. CONCLUSION

In this work, we have investigated the interplay between the NHSE and AL in a one-dimensional chain, where non-reciprocal hopping amplitudes drive the former, while quasiperiodic disorder induces the latter. Using an NH variant of the AA model, we explored the localization properties and analyzed its time evolution under single-site excitation. Additionally, we have analyzed the time evolution to reveal the occurrence of quantum jumps between skin states and Anderson localized states within the system. To bridge the gap between theory with experiment we have proposed a topoelectrical circuit as a realization of the model. Our findings highlight how the output voltage in such circuits can be precisely controlled using principles rooted in quantum localization phenomena. The competition between NHSE and AL manifests in a tangible and experimentally accessible manner, establishing electrical circuits as a powerful platform for studying such effects. This quantum-to-classical correspondence not only enhances our understanding of NHSE and AL but also paves the way for designing advanced sensors and efficient information transfer devices by leveraging the tunability and versatility of topoelectrical circuits.

Appendix A: Laplacian of the TEC

The TEC corresponding to the Hamiltonian, H (Eq. (1)), is constructed and analyzed in section IV A. For an electrical network with $2N + 1$ nodes, which is 21 for this case ($N = 10$), let \mathcal{L} represent the Laplacian, and V_i and I_i , respectively, de-

note the voltage and the total current from an external source at i^{th} node. Let us now derive the Laplacian of the circuit (refer to Fig. 3(b)) under the condition where the master switch

for S is open and S_1 is closed, representing the non-reciprocal circuit without the QP potential. Following Eq. (9) without any external source and the following $2N + 1$ equations,

$$\begin{aligned}
\frac{1}{j\omega L_{\text{edge}}} V_1 + j\omega(C - C')(V_1 - V_2) &= 0, \\
\frac{1}{j\omega L} V_2 + j\omega(C + C')(V_2 - V_1) + j\omega(C - C')(V_2 - V_3) &= 0, \\
&\vdots \\
\frac{1}{j\omega L'} V_{N+1} + j\omega(C + C')(V_{N+1} - V_N) + j\omega(C - C')(V_{N+1} - V_{N+2}) &= 0, \\
&\vdots \\
\frac{1}{j\omega L} V_{2N} + j\omega(C - C')(V_{2N} - V_{2N-1}) + j\omega(C + C')(V_{2N} - V_{2N+1}) &= 0, \\
\frac{1}{j\omega L_{\text{edge}}} V_L + j\omega(C - C')(V_{2N+1} - V_{2N}) &= 0,
\end{aligned}$$

where V_i is the voltage at i^{th} node, and the values of the circuit elements, C , C' , L , L' and L_{edge} are defined in the sections IV A and IV B. Note that j represents the imaginary number ($= \sqrt{-1}$) and $(N + 1)^{\text{th}}$ node denotes the interface. When we formulate these $2N + 1$ ($= 21$) equations corresponding to Kirchoff's law in the form $I = \mathcal{L}V$, the resulting Laplacian matrix, \mathcal{L} is given as,

$$\mathcal{L}(\omega) = \begin{pmatrix} \frac{1}{j\omega L_{\text{edge}}} + j\omega(C - C') & -j\omega(C - C') & 0 & \cdots & \cdots \\ -j\omega(C + C') & \frac{1}{j\omega L} + 2j\omega C & -j\omega(C - C') & 0 & \cdots \\ \vdots & \vdots & \vdots & \vdots & \vdots \\ \cdots 0 & -j\omega(C + C') & \frac{1}{j\omega L'} + 2j\omega(C + C') & -j\omega(C + C') & 0 \cdots \\ \vdots & \vdots & \vdots & \vdots & \vdots \\ \cdots & 0 & -j\omega(C - C') & \frac{1}{j\omega L} + 2j\omega C & -j\omega(C + C') \\ & \cdots & 0 & -j\omega(C - C') & \frac{1}{j\omega L_{\text{edge}}} + j\omega(C - C') \end{pmatrix}$$

Note that the diagonal terms vanish at the resonant frequency,

$$\omega_R = \frac{1}{\sqrt{2LC}} = \frac{1}{\sqrt{L_{\text{edge}}(C - C')}} = \frac{1}{\sqrt{2L'(C + C')}}.$$

Subsequently, at $\omega = \omega_R$, \mathcal{L} becomes,

$$\mathcal{L}(\omega_R) = -j \begin{pmatrix} 0 & \omega_R(C - C') & 0 & \cdots & \cdots \\ \omega_R(C + C') & 0 & \omega_R(C - C') & 0 & \cdots \\ \vdots & \vdots & \vdots & \vdots & \vdots \\ \cdots 0 & \omega_R(C + C') & 0 & \omega_R(C + C') & 0 \cdots \\ \vdots & \vdots & \vdots & \vdots & \vdots \\ \cdots & 0 & \omega_R(C - C') & 0 & \omega_R(C + C') \\ & \cdots & 0 & \omega_R(C - C') & 0 \end{pmatrix} \quad (\text{A1})$$

Thus, the Laplacian, \mathcal{L} , effectively replicates the matrix form of H with $\lambda = 0$, including a scaling factor of $-j$. Consequently, the eigenvalues and the eigenvectors of \mathcal{L} directly correspond to those of H with $\lambda = 0$. This equivalence ensures that the localization properties of the eigenvectors of the TB model are reflected in the VP derived from the Laplacian. Note that the capacitors are analogous to the hopping terms in

the TB model, where $(t \pm \gamma) \equiv \omega_R(C \pm C')$.

Now, let us incorporate the QP potential, as described in Eq. (1), into the TEC. This addition introduces extra diagonal terms in \mathcal{L} , stemming from the node-specific values of the capacitors, $C[k]$, and the resistors, $R[k]$ at the k^{th} node. Ac-

ording to Eq. (1), the QP potential is expressed as,

$$\begin{aligned}\lambda_k &= 2\lambda \cos(2\pi\beta k + i\alpha) \\ &= 2\lambda [\cos(2\pi\beta k) \cosh \alpha - i \sin(2\pi\beta k) \sinh \alpha].\end{aligned}$$

$$C[k] = -\text{Re}(\lambda_k)/\omega_R = -2\lambda \cos(2\pi\beta k) \cosh \alpha/\omega_R, \quad R[k] = [\text{Im}(\lambda_k)]^{-1} = [-2\lambda \sin(2\pi\beta k) \sinh \alpha]^{-1}.$$

After including these grounded capacitors and the resistors in Eq. (A1), \mathcal{L} assumes,

$$\mathcal{L} = -j \begin{pmatrix} -\omega_R C[1] + \frac{j}{R[1]} & \omega_R(C - C') & 0 & \dots & \dots & \dots \\ \omega_R(C + C') & -\omega_R C[2] + \frac{j}{R[2]} & \omega_R(C - C') & 0 & \dots & \dots \\ \vdots & \vdots & \vdots & \vdots & \vdots & \vdots \\ \dots 0 & \omega_R(C + C') & -\omega_R C[N+1] + \frac{j}{R[N+1]} & \omega_R(C + C') & 0 \dots & \dots \\ \vdots & \vdots & \vdots & \vdots & \vdots & \vdots \\ \dots & 0 & \omega_R(C - C') & -\omega_R C[2N] + \frac{j}{R[2N]} & \omega_R(C + C') & \dots \\ \dots & \dots & 0 & \omega_R(C - C') & -\omega_R C[2N+1] + \frac{j}{R[2N+1]} & \dots \end{pmatrix}. \quad (\text{A2})$$

Thus, Eqs. (A1) and (A2) represent the Laplacians for non-reciprocal TECs in the absence and presence of the complex QP disorder, respectively.

Appendix B: Theoretical time evolution of the TEC

Earlier, we have highlighted the difficulty of visualizing a specific eigenstate of the Laplacian, \mathcal{L} , as a measurable VP. This challenge arises because every node in the TEC network must be excited via a precisely calibrated current source. For example, to measure the k^{th} eigenstate of \mathcal{L} , denoted as V_k , the amplitude of the current source at each node must satisfy the equation,

$$I = \mathcal{L}V_k = \zeta_k V_k,$$

where ζ_k is the k^{th} eigenvalue of \mathcal{L} . To overcome this challenge, a current source, $I(t)$, can be applied at any node, and the VP ($V(t)$) can be measured at a later time. Similar to Eq. (3), $V(t)$ can also be expanded as a linear combination of the eigenvectors of \mathcal{L} , with time-dependent coefficients $a_k(t)$,

$$V(t) = \sum_{k=1} a_k(t) V_k. \quad (\text{B1})$$

We assume that V_k forms a complete orthonormal basis for \mathcal{L} with $V_a^\dagger V_b = \delta_{ab}$. Substituting these into Kirchhoff's law leads to,

$$\begin{aligned}I(t) &= \mathcal{L}V(t) = \sum_{k=1} a_k(t) \zeta_k V_k, \\ \Rightarrow a_k(t) &= \frac{V_k^\dagger I(t)}{\zeta_k}.\end{aligned} \quad (\text{B2})$$

Thus, at the resonant frequency, ω_R , $C[k]$ and $R[k]$ assume following forms,

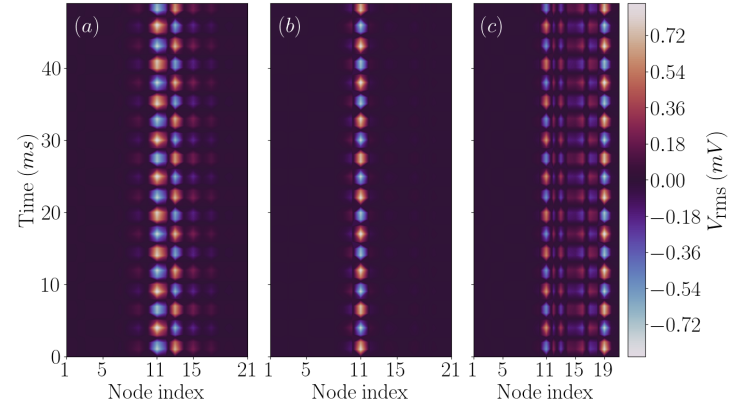


FIG. 7. (a) The NHSE is evident as the $V(t)$ localizes at the interface, specifically at 11th node. (b) When $\alpha = \alpha_c$, all the eigenstates of the Laplacian \mathcal{L} transform from the skin states to the AL states, yet the VP remains localized at the interface. (c) Finally, for a larger value of α , the localization shifts towards the excitation node, which is the 18th node.

Thus, the coefficients $a_k(t)$ can be evaluated at any time t , provided the input current $I(t)$ is uniquely defined. The expression for $a_k(t)$ in Eq.(B2) becomes directly comparable to the coefficients $a_q(t)$ in Eq.(4) only when $I(t)$ takes the form of a delta-type excitation, that is, a sharply peaked current pulse with very high amplitude at $t = 0$ and vanishingly short duration. Only under this condition does the time evolution of the VP in Eq.(B1) accurately correspond to the evolution of the wavefunction $|\Psi(x, t)\rangle$ described in Eq.(6). However, to study the dynamical behavior of the TEC, we resort to a specific case and excite the 18th node with a current source, $I(t) = \sin \omega_R t$, having an amplitude of 1 mA and ω_R rep-

representing the resonant frequency of the circuit. By employing Eqs. (B1) and (B2), we obtain $V(t)$, which is then represented as a colormap in Fig. 7. Figs.7(a) and (b) illustrate the scenario for $\alpha \leq \alpha_c$, where the NHSE still dominates over AL in the TEC. This behavior mirrors that of the NH AA model in Figs.2(a) and (b), as the excitation remains localized at the in-

terface (the 11th node). However, compared to Fig.2(c) for the case of TB model, no NH jumps are observed in the TEC, as seen in Fig.7(c). This difference arises because the input current $I(t)$ in the circuit is a sinusoidal function of time, rather than a delta-type excitation. Instead, the VP settles at the 19th node, located in the vicinity of the excitation (18th) node.

-
- [1] P. W. Anderson, Absence of diffusion in certain random lattices, *Phys. Rev.* **109**, 1492 (1958).
- [2] S. Aubry and G. André, Analyticity breaking and anderson localization in incommensurate lattices, *Ann. Isr. Phys. Soc.* **3** (1980).
- [3] S. Ganeshan, K. Sun, and S. Das Sarma, Topological zero-energy modes in gapless commensurate aubry-andré-harper models, *Phys. Rev. Lett.* **110**, 180403 (2013).
- [4] S. Ganeshan, J. H. Pixley, and S. Das Sarma, Nearest neighbor tight binding models with an exact mobility edge in one dimension, *Phys. Rev. Lett.* **114**, 146601 (2015).
- [5] G. De Tomasi, S. Bera, J. H. Bardarson, and F. Pollmann, Quantum mutual information as a probe for many-body localization, *Phys. Rev. Lett.* **118**, 016804 (2017).
- [6] Y. Lahini, R. Pugatch, F. Pozzi, M. Sorel, R. Morandotti, N. Davidson, and Y. Silberberg, Observation of a localization transition in quasiperiodic photonic lattices, *Phys. Rev. Lett.* **103**, 013901 (2009).
- [7] Y. E. Kraus, Y. Lahini, Z. Ringel, M. Verbin, and O. Zeitler, Topological states and adiabatic pumping in quasicrystals, *Phys. Rev. Lett.* **109**, 106402 (2012).
- [8] S. Dey, N. R. Das, and S. Ghosh, Exploring unconventional features of light dynamics in aubrey-andré-harper model based quasi-periodic optical lattices, *Optics Communications* **506**, 127593 (2022).
- [9] G. Roati, C. D'Errico, L. Fallani, M. Fattori, C. Fort, M. Zaccanti, G. Modugno, M. Modugno, and M. Inguscio, Anderson localization of a non-interacting bose-einstein condensate, *Nature* **453**, 895 (2008).
- [10] F. A. An, K. Padavić, E. J. Meier, S. Hegde, S. Ganeshan, J. H. Pixley, S. Vishveshwara, and B. Gadway, Interactions and mobility edges: Observing the generalized aubry-andré model, *Phys. Rev. Lett.* **126**, 040603 (2021).
- [11] H. Li, Y.-Y. Wang, Y.-H. Shi, K. Huang, X. Song, G.-H. Liang, Z.-Y. Mei, B. Zhou, H. Zhang, J.-C. Zhang, S. Chen, S. P. Zhao, Y. Tian, Z.-Y. Yang, Z. Xiang, K. Xu, D. Zheng, and H. Fan, Observation of critical phase transition in a generalized aubry-andré-harper model with superconducting circuits, *npj Quantum Information* **9**, 40 (2023).
- [12] T. E. Lee, Anomalous edge state in a non-hermitian lattice, *Phys. Rev. Lett.* **116**, 133903 (2016).
- [13] H. Shen, B. Zhen, and L. Fu, Topological band theory for non-hermitian hamiltonians, *Phys. Rev. Lett.* **120**, 146402 (2018).
- [14] Y. Ashida, Z. Gong, and M. Ueda, Non-hermitian physics, *Advances in Physics* **69**, 249 (2020).
- [15] E. J. Bergholtz, J. C. Budich, and F. K. Kunst, Exceptional topology of non-hermitian systems, *Rev. Mod. Phys.* **93**, 015005 (2021).
- [16] S. Yao and Z. Wang, Edge states and topological invariants of non-hermitian systems, *Phys. Rev. Lett.* **121**, 086803 (2018).
- [17] C. H. Lee and R. Thomale, Anatomy of skin modes and topology in non-hermitian systems, *Phys. Rev. B* **99**, 201103 (2019).
- [18] N. Okuma, K. Kawabata, K. Shiozaki, and M. Sato, Topological origin of non-hermitian skin effects, *Phys. Rev. Lett.* **124**, 086801 (2020).
- [19] D. S. Borgnia, A. J. Kruchkov, and R.-J. Slager, Non-hermitian boundary modes and topology, *Phys. Rev. Lett.* **124**, 056802 (2020).
- [20] M.-H. L. Xiujuan Zhang, Tian Zhang and Y.-F. Chen, A review on non-hermitian skin effect, *Advances in Physics: X* **7**, 2109431 (2022).
- [21] W. D. Heiss, The physics of exceptional points, *Journal of Physics A: Mathematical and Theoretical* **45**, 444016 (2012).
- [22] D. Leykam, K. Y. Bliokh, C. Huang, Y. D. Chong, and F. Nori, Edge modes, degeneracies, and topological numbers in non-hermitian systems, *Phys. Rev. Lett.* **118**, 040401 (2017).
- [23] K. Yokomizo and S. Murakami, Non-bloch band theory of non-hermitian systems, *Phys. Rev. Lett.* **123**, 066404 (2019).
- [24] T. Eichelkraut, R. Heilmann, S. Weimann, S. Stützer, F. Dreisow, D. N. Christodoulides, S. Nolte, and A. Szameit, Mobility transition from ballistic to diffusive transport in non-hermitian lattices, *Nature Communications* **4**, 2533 (2013).
- [25] R. El-Ganainy, K. G. Makris, M. Khajavikhan, Z. H. Musslimani, S. Rotter, and D. N. Christodoulides, Non-hermitian physics and pt symmetry, *Nature Physics* **14**, 11 (2018).
- [26] A. Wang, Z. Meng, and C. Q. Chen, Non-hermitian topology in static mechanical metamaterials, *Science Advances* **9** (2023).
- [27] R. Fleury, D. Sounas, and A. Alù, An invisible acoustic sensor based on parity-time symmetry, *Nat. Commun.* **6**, 10.1038/ncomms6905 (2015).
- [28] T. Guo, B. Assouar, B. Vincent, and A. Merkel, Edge states in non-hermitian composite acoustic su schrieffer heeger chains, *Journal of Applied Physics* **135**, 043102 (2024).
- [29] M. Peng, C. Wu, Z. Cui, X. Zhang, Q. Wei, M. Yan, and G. Chen, Acoustic non-hermitian dirac states tuned by flexible designed gain and loss, *Applied Physics Letters* **125**, 193101 (2024).
- [30] N. Hatano and D. R. Nelson, Localization transitions in non-hermitian quantum mechanics, *Phys. Rev. Lett.* **77**, 570 (1996).
- [31] S. Longhi, Topological phase transition in non-hermitian quasicrystals, *Phys. Rev. Lett.* **122**, 237601 (2019).
- [32] S. Schiffer, X.-J. Liu, H. Hu, and J. Wang, Anderson localization transition in a robust \mathcal{PT} -symmetric phase of a generalized aubry-andré model, *Phys. Rev. A* **103**, L011302 (2021).
- [33] S. Longhi, Phase transitions in a non-hermitian aubry-andré-harper model, *Phys. Rev. B* **103**, 054203 (2021).
- [34] Y. Liu, Q. Zhou, and S. Chen, Localization transition, spectrum structure, and winding numbers for one-dimensional non-hermitian quasicrystals, *Phys. Rev. B* **104**, 024201 (2021).
- [35] X. Cai, Localization transitions and winding numbers for non-hermitian aubry-andré-harper models with off-diagonal modulations, *Phys. Rev. B* **106**, 214207 (2022).
- [36] S. Gandhi and J. N. Bandyopadhyay, Topological triple phase transition in non-hermitian quasicrystals with complex asymmetric hopping, *Phys. Rev. B* **108**, 014204 (2023).

- [37] Y.-M. Sun, X.-Y. Wang, and L.-J. Zhai, Hybrid scaling properties of the localization transition in a non-hermitian disordered aubry-andré model, *Phys. Rev. B* **110**, 054202 (2024).
- [38] S.-Z. Li, E. Cheng, S.-L. Zhu, and Z. Li, Asymmetric transfer matrix analysis of lyapunov exponents in one-dimensional nonreciprocal quasicrystals, *Phys. Rev. B* **110**, 134203 (2024).
- [39] V. V. Albert, L. I. Glazman, and L. Jiang, Topological properties of linear circuit lattices, *Phys. Rev. Lett.* **114**, 173902 (2015).
- [40] C. H. Lee, S. Imhof, C. Berger, F. Bayer, J. Brehm, L. W. Molenkamp, T. Kiessling, and R. Thomale, Topoelectrical circuits, *Communications Physics* **1**, 39 (2018).
- [41] T. Helbig, T. Hofmann, C. H. Lee, R. Thomale, S. Imhof, L. W. Molenkamp, and T. Kiessling, Band structure engineering and reconstruction in electric circuit networks, *Phys. Rev. B* **99**, 161114 (2019).
- [42] J. Dong, V. Juričić, and B. Roy, Topoelectric circuits: Theory and construction, *Phys. Rev. Res.* **3**, 023056 (2021).
- [43] S. Guo, G. Pan, J. Huang, R. Huang, F. Zhuang, S. Su, Z. Lin, W. Qiu, and Q. Kan, Realization of the square-root higher-order topology in decorated su–schrieffer–heeger electric circuits, *Applied Physics Letters* **123**, 043102 (2023).
- [44] H. Yang, L. Song, Y. Cao, and P. Yan, Circuit realization of topological physics, *Physics Reports* **1093**, 1 (2024), circuit realization of topological physics.
- [45] T. Helbig, T. Hofmann, S. Imhof, M. Abdelghany, T. Kiessling, L. W. Molenkamp, C. H. Lee, A. Szameit, M. Greiter, and R. Thomale, Generalized bulk–boundary correspondence in non-hermitian topoelectrical circuits, *Nature Physics* **16**, 747 (2020).
- [46] B. Liu, Y. Li, B. Yang, X. Shen, Y. Yang, Z. H. Hang, and M. Ezawa, Experimental observation of non-hermitian higher-order skin interface states in topological electric circuits, *Phys. Rev. Res.* **5**, 043034 (2023).
- [47] W. Lin, B. Ruan, C. Liu, X. Dai, and Y. Xiang, Evolution of topological extended state in multidimensional non-hermitian topoelectrical circuits, *Applied Physics Letters* **125**, 173104 (2024).
- [48] D. Halder, R. Thomale, and S. Basu, Circuit realization of a two-orbital non-hermitian tight-binding chain, *Phys. Rev. B* **109**, 115407 (2024).
- [49] C.-X. Guo, L. Su, Y. Wang, L. Li, J. Wang, X. Ruan, Y. Du, D. Zheng, S. Chen, and H. Hu, Scale-tailored localization and its observation in non-hermitian electrical circuits, *Nature Communications* **15**, 9120 (2024).
- [50] S. M. Rafi-UI-Islam, Z. B. Siu, M. S. H. Razo, and M. B. A. Jalil, [Dynamic manipulation of non-hermitian skin effect through frequency in topoelectrical circuits](#) (2024), [arXiv:2410.16914 \[cond-mat.mes-hall\]](#).
- [51] H. Jiang, L.-J. Lang, C. Yang, S.-L. Zhu, and S. Chen, Interplay of non-hermitian skin effects and anderson localization in nonreciprocal quasiperiodic lattices, *Phys. Rev. B* **100**, 054301 (2019).
- [52] Q.-B. Zeng and Y. Xu, Winding numbers and generalized mobility edges in non-hermitian systems, *Phys. Rev. Res.* **2**, 033052 (2020).
- [53] X. Xia, K. Huang, S. Wang, and X. Li, Exact mobility edges in the non-hermitian t_1-t_2 model: Theory and possible experimental realizations, *Phys. Rev. B* **105**, 014207 (2022).
- [54] S. Ganguly and S. K. Maiti, Electrical analogue of one-dimensional and quasi-one-dimensional aubry–andré–harper lattices, *Scientific Reports* **13**, 13633 (2023).
- [55] H. Wang, W. Zhang, H. Sun, and X. Zhang, Observation of non-abelian anderson localization and transition in topoelectrical circuits, *Phys. Rev. B* **108**, 144203 (2023).
- [56] To know more, please visit the following link: [LTspice](#).
- [57] In usual notation, the localization-delocalization transition occurs at $\lambda = 2t$. However, we have absorbed a factor of 2 in the QP potential in Eq. (1).
- [58] A. Avila, Global theory of one-frequency Schrödinger operators, *Acta Mathematica* **215**, 1 (2015).
- [59] A. Chakrabarty and S. Datta, Skin effect and dynamical delocalization in non-hermitian quasicrystals with spin-orbit interaction, *Phys. Rev. B* **107**, 064305 (2023).
- [60] S. Weidemann, M. Kremer, S. Longhi, and A. Szameit, Coexistence of dynamical delocalization and spectral localization through stochastic dissipation, *Nature Photonics* **15**, 576 (2021).
- [61] A. F. Tzortzakakis, K. G. Makris, A. Szameit, and E. N. Economou, Transport and spectral features in non-hermitian open systems, *Phys. Rev. Res.* **3**, 013208 (2021).
- [62] A. Leventis, K. G. Makris, and E. N. Economou, Non-hermitian jumps in disordered lattices, *Phys. Rev. B* **106**, 064205 (2022).
- [63] F. Y. Wu, Theory of resistor networks: the two-point resistance, *Journal of Physics A: Mathematical and General* **37**, 6653 (2004).
- [64] S. Weidemann, M. Kremer, T. Helbig, T. Hofmann, A. Stegmaier, M. Greiter, R. Thomale, and A. Szameit, Topological funneling of light, *Science* **368**, 311 (2020).